Acta Mech. Sin. (2011) 27(4):473–487
DOI 10.1007/s10409-011-0475-3

RESEARCH PAPER

Turbulence and cavitation models for time-dependent turbulent cavitating flows

Ying-Jie Wei · Chien-Chou Tseng · Guo-Yu Wang

Received: 30 June 2010 / Revised: 23 December 2010 / Accepted: 23 December 2010

Abstract Cavitation typically occurs when the fluid pressure is lower than the vapor pressure at a local thermodynamic state, and the flow is frequently unsteady and turbulent. To assess the state-of-the-art of computational capabilities for unsteady cavitating flows, different cavitation and turbulence model combinations are conducted. The selected cavitation models include several widely-used models including one based on phenomenological argument and the other utilizing interface dynamics. The k-ε turbulence model with additional implementation of the filter function and density correction function are considered to reduce the eddy viscosity according to the computed turbulence length scale and local fluid density respectively. We have also blended these alternative cavitation and turbulence treatments, to illustrate that the eddy viscosity near the closure region can significantly influence the capture of detached cavity. From the experimental validations regarding the force analysis, frequency, and the cavity visualization, no single model combination performs best in all aspects. Furthermore, the implications of parameters contained in different cavitation models are investigated. The phase change process is more pronounced around the detached cavity, which is better illustrated by the interfacial dynamics model. Our study provides insight to aid further modeling development.

Keywords Cavitation · Turbulence model · Cavitation model · Hybrid model

Nomenclature

σ	Local cavitation number; cavitation number based on the local temperature
$C_{\varepsilon 1}, C_{\varepsilon 2}, \sigma_\varepsilon, \sigma_k$	Coefficients of k-ε turbulence model
C	Chord length of hydrofoil
L	Characteristic length scale
I	Turbulence intensity
k	Turbulent kinetic energy
$\dot{m}^+, \dot{m}^-$	Source and sink terms in the cavitation model
p	Pressure
p_v	Saturation vapor pressure
Re	Reynolds number
t_∞	Reference time scale, $t_\infty = L/U_\infty$
U_∞	Reference velocity scale
u	Velocity
$U_{\mathrm{v},n}$	Normal component of the vapor velocity moving away from the interface
$U_{\mathrm{I},n}$	Normal interfacial velocity
x	Space variable
α_l	Liquid volume fraction
ρ	Density
μ	Dynamic viscosity
$\mu_\mathrm{T}/\mu_\mathrm{L}\vert_\mathrm{inlet}$	Eddy-to-laminar viscosity ratio at the inlet
ϕ_m	Mixture property
ε	Turbulent dissipation rate
Δ	Filter size in filter-based model

1 Introduction

Cavitation typically occurs when the fluid pressure is lower than the vapor pressure at a local thermodynamic state [1–5]. It is often associated with undesired effects, such as noise,

---

The project was supported by the National Natural Science Foundation of China (10802026).

Y.-J. Wei (✉)
School of Astronautics, Harbin Institute of Technology,
150001 Harbin, China
e-mail: weiyingjie@gmail.com

C.-C. Tseng
Department of Mechanical Engineering,
University of Michigan, 2350 Hayward,
Ann Arbor, MI 48109, USA

G.-Y. Wang
School of Vehicle and Transportation Engineering,
Beijing Institute of Technology, 100081 Beijing, China

vibration, erosion, and power loss. Cavitation can happen in all kinds of fluid machinery components, such as nozzles, injectors, propellers, and hydrofoil.

As cavitation occurs, the forming vapor phase will replace the liquid phase inside the cavity, and in order to maintain the vapor phase, the surrounding liquid will adjust its thermodynamic state and experience evaporative cooling, which causes temperature drop around the cavity. For fluids such as water, due to a very large ratio between liquid and vapor densities, around $O(10^5)$, these thermal effects are insignificant during cavitation process.

Experimentally, the unsteadiness and turbulence interactions have been investigated in multiple researches. It has been demonstrated that the convection essence of cavitation and the unsteady structure of cloud cavitation can occur even the hydrofoil is stationary with steady inlet conditions [6]. For the cloud cavitation, the pressure coefficient experiences an adverse pressure gradient at the closure region. It has been found out that the intensity of pressure fluctuations is clearly larger in the area close to the closure region. As the cavitation number decreases, and the cavity length increases, the fluctuations also become larger with a bigger affected area [7]. Furthermore, it has been demonstrated that re-entrant jet after the closure region is the basic mechanism that triggers the shedding of the cloud cavitation. The re-entrant jet is from the trailing edge to the leading edge of the sheet cavity. Therefore, the re-entrant jet is not the propagation of the collapse of the sheet cavity, but is a flow under a sheet cavity [8]. Furthermore, cavitation instability induced by the development of a re-entrant jet for water past a back step channel is studied [9], and the re-entrant jet will be created if the adverse pressure gradient near the closure region is large enough. Gopalan et al. [10] have demonstrated that the collapse of vapor bubbles in the closure region for sheet cavitation is the primary source of vorticity production. Besides, the change in the size of cavity will result in significant changes in turbulence level and momentum thickness of the downstream boundary layer. Li et al. [11] have shown that traveling bubbles close to the surface can induce local turbulent regions by stretching the boundary layer and will also create streamwise vorticity.

Various cavitation models can be categorized based on how the moving interface and multiphase mixtures are handled, namely, (1) interface tracking method [12,13]; (2) coupled density and pressure models [14–16]; (3) transport models [17–29] for liquid/mass fraction. In the first category, Chen et al. [12] and Deshpande et al. [13] have treated the computational domains with individual phases separately by time-wise grid regeneration according to the cavity shape. The pressure inside the cavity is considered constant, and a wake model is used to handle the cavity closure. This method is insufficient once the cavity is detached. In the second category, the homogeneous flow models based on a single-fluid framework with fluid properties estimated based on the liquid-vapor mixture ratios are used. Without additional cavitation model, density will be directly coupled with pressure by some specific equations, such as equations of states [14,15]. If the pressure is iterated, the saturation temperature can be interpolated, and then the enthalpy and the specific volume along the saturation water and vapor line can be updated. In this way, the iterated enthalpy can determine if the substance is in vapor, liquid or mixture phase, and then each phase has its own equation of state to specify the density. Delannoy et al. [16] have also utilized the arbitrary barotropic equations to solve the density field. However, these approaches in this (second) category fail to capture some fundamental fluid physics such as baroclinic vorticity production, which has been shown in experimental study [10]. In reality, the pressure and density gradients are not always parallel. For these kinds of methods, they can not account for the convection and transport phenomenon of the cavitation bubbles due to the lack of cavitation transport equation, and hence these models will be more suitable for attached cavity.

In this study, we focus on the third category with transport-based cavitation models. A popular homogeneous flow model utilizes the framework of the transport-based equation (TEM) [17–28], which is adopted in the present study. In this method, the information of the vapor volume/mass fraction distribution is obtained in a modeled transport equation based on the mass transfer between vapor and liquid phases. The cavitation sink and source terms can be derived based on (1) the phenomenological model employing dimensional argument and semi-empirical guidance [17–25]; (2) the interfacial dynamics model based on transport laws across phase boundaries [21,22]; and (3) the Rayliegh-Plesset equation for bubble dynamics [26–29]. We will have detail descriptions for the phenomenological and interfacial dynamics model in the next section. As for those models that utilize the simplified Rayliegh-Plesset equation, the assumptions, such as constant bubble number density and arbitrary constant that replaces the bubble number density, have limited the accuracy.

For turbulence, the ensemble-averaged modeling with a two-equation closure along with a filter-based model (FBM) [17,23–25,30] is utilized. The approach reduces the influence of the turbulent eddy viscosity based on the local numerical resolution, essentially blending direct numerical simulation (DNS) and conventional turbulence model in a single framework. Specifically, the level of the turbulent viscosity is corrected by comparing the turbulence length scale computed from the turbulence closure and the filter size Δ based on the local mesh spacing. As discussed in Ref. [24], the uncertainty associated with inlet turbulent quantities can substantially impact the outcome of the conventional two-equation eddy viscosity model. The filter-based approach can effectively improve the consistency of the numerical predictions by reducing the reliance on the turbulence closure. Furthermore, to account for the large density jump caused by cavitation, research in Refs. [20,27,30] has considered the compressibility of mixture phases by a density correction function. Under this treatment, the reduced eddy viscosity can capture the unsteadiness and re-entrant based on the mixture density.

The present study is aimed at addressing the modeling interaction between cavitation and turbulence by comparing with experimental data, and provide the insightful information for further modeling modifications.

2 Governing equations and numerical techniques

The set of governing equations for isothermal cavitation under the homogeneous-fluid modeling consists of the conservative form of the Favre-averaged Navier–Stokes equations, the k-ε two-equation turbulence closure, and a transport equation for the liquid volume fraction [24,25]. The continuity, momentum, and cavitation model equations are given below

$$\frac{\partial \rho_{\mathrm{m}}}{\partial t}+\frac{\partial(\rho_{\mathrm{m}} u_j)}{\partial x_j}=0, \tag{1}$$

$$\frac{\partial(\rho_{\mathrm{m}} u_i)}{\partial t}+\frac{\partial(\rho_{\mathrm{m}} u_i u_j)}{\partial x_j} = -\frac{\partial p}{\partial x_i}+\frac{\partial}{\partial x_j}\left[(\mu_{\mathrm{L}}+\mu_{\mathrm{T}})\left(\frac{\partial u_i}{\partial x_j}+\frac{\partial u_j}{\partial x_i}-\frac{2}{3}\frac{\partial u_k}{\partial x_k}\delta_{ij}\right)\right], \tag{2}$$

$$\frac{\partial \alpha_{\mathrm{l}}}{\partial t}+\frac{\partial(\alpha_{\mathrm{l}} u_j)}{\partial x_j}=\dot{m}^{+}+\dot{m}^{-}. \tag{3}$$

The mixture property, ϕ_{m}, can be expressed as

$$\phi_{\mathrm{m}}=\phi_{\mathrm{l}}\alpha_{\mathrm{l}}+\phi_{\mathrm{v}}(1-\alpha_{\mathrm{l}}), \tag{4}$$

where ϕ can be density, viscosity, and so on.

2.1 Transport-based cavitation model

The source term $\dot{m}^{+}$ and sink term $\dot{m}^{-}$ in Eq. (4) represent the condensation and evaporation rates. A popular phenomenological model, originally proposed by Merkle et al. [18] and investigated by numerous researchers with modified model parameters [17,19–25], resulted largely from the dimensional argument. The representative liquid-vapor evaporation and condensation rates for this category are shown as following

$$\begin{aligned}\dot{m}^{-}&=\frac{C_{\mathrm{dest}}\rho_{\mathrm{l}}\min(p-p_{\mathrm{v}},0)\alpha_{\mathrm{l}}}{\rho_{\mathrm{v}}(0.5\rho_{\mathrm{l}}U_{\infty}^{2})t_{\infty}},\\ \dot{m}^{+}&=\frac{C_{\mathrm{prod}}\max(p-p_{\mathrm{v}},0)(1-\alpha_{\mathrm{l}})}{(0.5\rho_{\mathrm{l}}U_{\infty}^{2})t_{\infty}}.\end{aligned} \tag{5}$$

The conditional statement in the source term $\dot{m}^{+}$ and sink term $\dot{m}^{-}$ means evaporation/condensation occurs when pressure is lower/higher than vapor pressure under the assumption of thermal equilibrium.

In Eq. (6), C_{dest} and C_{prod} are the empirical constants, U_{∞} is the reference velocity scale, and t_{∞} is the reference time scale, which is defined as the characteristic length scale L divided by the reference velocity scale U_{∞} ($t_{\infty}=L/U_{\infty}$). As the results, the models here are derived for entire bubble clusters, but not a single bubble. For non-cryogenic fluids like water, different constants are specified [18,21,31]. $C_{\mathrm{dest}}=C_{\mathrm{prod}}=1\,000$ are originally used by Merkle et al. [18] to solve the vapor mass fraction. $C_{\mathrm{dest}}=1$ and $C_{\mathrm{prod}}=80$ used by Secnocak et al. [21] are adopted in this study. However, these values are materials dependent and different for, e.g., liquid nitrogen and hydrogen under cryogenic condition [17, 21–25].

Senocak and Shyy [21,22] have developed the interfacial dynamics model (IDM) by considering the interfacial dynamics, at high Reynolds number approximation neglecting the viscous and surface tension forces. Based on the continuity and force balance on the interfacial dynamics, one obtains the following equations

$$\rho_{\mathrm{l}}(U_{\mathrm{l},n}-U_{\mathrm{I},n})=\rho_{\mathrm{v}}(U_{\mathrm{v},n}-U_{\mathrm{I},n}), \tag{6}$$

$$p_{\mathrm{v}}-p_{\mathrm{l}}=\rho_{\mathrm{l}}(U_{\mathrm{l},n}-U_{\mathrm{I},n})^{2}-\rho_{\mathrm{v}}(U_{\mathrm{v},n}-U_{\mathrm{I},n})^{2}. \tag{7}$$

In the next step, it is considered that the phase change takes place between mixture and vapor phases across clear interfaces by simply replacing the liquid phase with mixture phase. Furthermore, the following cavitation sink and source term can be obtained by combining Eqs. (4), (6) and (7) for mixture density, and normalizing the combined equation with t_{∞}

$$\begin{aligned}\dot{m}^{-}&=\frac{\rho_{\mathrm{l}}\min(p-p_{\mathrm{v}},0)\alpha_{\mathrm{l}}}{\rho_{\mathrm{v}}(U_{\mathrm{v},n}-U_{\mathrm{I},n})^{2}(\rho_{\mathrm{l}}-\rho_{\mathrm{v}})t_{\infty}},\\ \dot{m}^{+}&=\frac{\max(p-p_{\mathrm{v}},0)(1-\alpha_{\mathrm{l}})}{(U_{\mathrm{v},n}-U_{\mathrm{I},n})^{2}(\rho_{\mathrm{l}}-\rho_{\mathrm{v}})t_{\infty}}.\end{aligned} \tag{8}$$

The choice of the time scale in Eq. (8) depends on the cavitation dynamics. A systematic investigation is needed to ascertain this aspect. In the present study, it is chosen as L/U_{∞} as that in Eq. (5) for the entire bubble clusters.

The empirical constants in Eq. (5) now can be replaced by the explicit calculations for the interfacial velocity terms here, the normal component of the vapor velocity moving away from the interface, $U_{\mathrm{v},n}$, is calculated as

$$U_{\mathrm{v},n}=\frac{\nabla\alpha_{\mathrm{l}}}{|\nabla\alpha_{\mathrm{l}}|}\cdot u. \tag{9}$$

The normal interfacial velocity, $U_{\mathrm{I},n}$, is zero in steady calculation. However, in unsteady computations this term needs modeling efforts. Previous studies expressed $U_{\mathrm{I},n}$ in terms of part of the $U_{\mathrm{v},n}$ [17,21–23]. An alternate method of modeling is also discussed by Wu et al. [17,23], which is based on the local variation of liquid volume fraction with time marching

$$U_{\mathrm{I},n}=\frac{\Delta\dot{m}}{S}=\frac{[\alpha_{\mathrm{l}}(t+\Delta t)-\alpha_{\mathrm{l}}(t)]\cdot S_{\mathrm{CV}}}{\Delta t\cdot S}, \tag{10}$$

where S_{CV} is the control volume face area; S is the interface area, and it can be calculated by projection of control volume face area to the normal direction of interface, which can be obtained by taking the gradient of the volume fraction.

$$S = \frac{S_{\mathrm{CV}}}{\left| n_x \Big/ \sqrt{n_x^2 + n_y^2} \right|}, \qquad \boldsymbol{n} = \frac{\nabla \alpha_{\mathrm{l}}}{|\nabla \alpha_{\mathrm{l}}|} = n_x \boldsymbol{i} + n_y \boldsymbol{j}\,. \tag{11}$$

In current study, we will utilize the phenomenological cavitation model and IDM (shown in Table 1) to investigate the impacts of cavitation models.

Table 1 Cavitation models used in the present study

Model	Source term	Sink term
Phenomenological model	$\dfrac{C_{\mathrm{prod}} \max(p - p_{\mathrm{v}}, 0)(1 - \alpha_{\mathrm{l}})}{(0.5\rho_{\mathrm{l}} U_\infty^2) t_\infty}$	$\dfrac{C_{\mathrm{dest}} \rho_{\mathrm{l}} \min(p - p_{\mathrm{v}}, 0)\alpha_{\mathrm{l}}}{\rho_{\mathrm{v}}(0.5\rho_{\mathrm{l}} U_\infty^2) t_\infty}$
	$C_{\mathrm{prod}} = 1$	$C_{\mathrm{dest}} = 80$
Interfacial dynamics model (IDM)	$\dfrac{\max(p - p_{\mathrm{v}}, 0)(1 - \alpha_{\mathrm{l}})}{(\rho_{\mathrm{l}} - \rho_{\mathrm{v}})(U_{\mathrm{v},n} - U_{\mathrm{I},n})^2 t_\infty}$	$\dfrac{C_{\mathrm{dest}} \rho_{\mathrm{l}} \min(p - p_{\mathrm{v}}, 0)\alpha_{\mathrm{l}}}{\rho_{\mathrm{v}}(\rho_{\mathrm{l}} - \rho_{\mathrm{v}})(U_{\mathrm{v},n} - U_{\mathrm{I},n})^2 t_\infty}$

2.2 Turbulence model

The k-ε two-equation turbulence model with a wall function treatment is presented as follows [32,33]

$$\frac{\partial(\rho_{\mathrm{m}} k)}{\partial t} + \frac{\partial(\rho_{\mathrm{m}} k u_j)}{\partial x_j} = P_{\mathrm{t}} - \rho_{\mathrm{m}} \varepsilon + \frac{\partial}{\partial x_j}\left[\left(\mu_{\mathrm{L}} + \frac{\mu_{\mathrm{T}}}{\sigma_k}\right)\frac{\partial k}{\partial x_j}\right], \tag{12}$$

$$\frac{\partial(\rho_{\mathrm{m}} \varepsilon)}{\partial t} + \frac{\partial(\rho_{\mathrm{m}} \varepsilon u_j)}{\partial x_j} = C_{\varepsilon 1} \frac{\varepsilon}{k} P_{\mathrm{t}} - C_{\varepsilon 2} \rho_{\mathrm{m}} \frac{\varepsilon^2}{k} + \frac{\partial}{\partial x_j}\left[\left(\mu_{\mathrm{L}} + \frac{\mu_{\mathrm{T}}}{\sigma_\varepsilon}\right)\frac{\partial \varepsilon}{\partial x_j}\right], \tag{13}$$

where the production term of turbulent kinetic energy (P_t) and the Reynolds stress tensor (τ_{ij}) are defined as

$$P_{\mathrm{t}} = \tau_{ij} \frac{\partial u_i}{\partial x_j}, \tag{14}$$

$$\tau_{ij} = -\rho_{\mathrm{m}} u_i' u_j' = \frac{2}{3} \rho_{\mathrm{m}} k \delta_{ij} - \mu_{\mathrm{T}}\left(\frac{\partial u_i}{\partial x_j} + \frac{\partial u_j}{\partial x_i}\right), \tag{15}$$

with $C_{\varepsilon 1} = 1.44$, $C_{\varepsilon 2} = 1.92$, $\sigma_{\varepsilon 1} = 1.3$, $\sigma_k = 1.0$. The turbulent eddy viscosity is defined as

$$\mu_{\mathrm{T}} = \frac{C_\mu \rho_{\mathrm{m}} k^2}{\varepsilon}, \qquad C_\mu = 0.09. \tag{16}$$

As mentioned in previous section, a filter-based model (FBM) [17,23–25,34] is also adopted. This model limits the influence of the eddy viscosity based on the local numerical resolution, essentially forming a combined direct numerical simulation and RANS model. Specifically, the level of the turbulent viscosity is corrected by comparing the turbulence length scale and the filter size $\varDelta$, which is based on the local meshing spacing

$$\begin{aligned} &\mu_{\mathrm{T\_FBM}} = \frac{C_\mu \rho_{\mathrm{m}} k^2}{\varepsilon} f_{\mathrm{FBM}}, \\ &C_\mu = 0.09, \\ &f_{\mathrm{FBM}} = \min\left(1, \frac{\varDelta \cdot \varepsilon}{k^{3/2}}\right). \end{aligned} \tag{17}$$

By imposing the filter, the turbulence length scale will not be resolved if it is smaller than the filter size. The filter size is chosen to be comparable to the maximum grid size.

$$\varDelta = \max(\varDelta_{\mathrm{present}}, \varDelta_{\mathrm{grid}}). \tag{18}$$

Thus if the grid resolution is significantly smaller than the turbulence length scale in the entire flow field, the solution will approach that of a direct numerical simulation; for inadequately resolved computations, the RANS model is recovered. With the appearance of the filter function in Eq. (17), the sensitivity due to inlet turbulent quantities are reduced [24,25].

To account for the large density jump caused by cavitation and re-entrant jet near the closure region, researches in Refs. [20,27,30] have considered the compressibility of mixture phases and used a density correction based model (DCM), and modified the eddy viscosity as

$$\begin{aligned} &\mu_{\mathrm{T\_DCM}} = \frac{C_\mu \rho_{\mathrm{m}} k^2}{\varepsilon} f_{\mathrm{DCM}}, \\ &C_\mu = 0.09, \\ &f_{\mathrm{DCM}} = \frac{\rho_{\mathrm{v}} + (\alpha_{\mathrm{l}})^n (\rho_{\mathrm{l}} - \rho_{\mathrm{v}})}{\rho_{\mathrm{v}} + \alpha_{\mathrm{l}}(\rho_{\mathrm{l}} - \rho_{\mathrm{v}})}. \end{aligned} \tag{19}$$

With such a treatment, the eddy viscosity is reduced based on the liquid volume fraction, as shown in Fig. 1 with $n = 10$, and can be used to capture the unsteadiness due to the re-entrant jet.

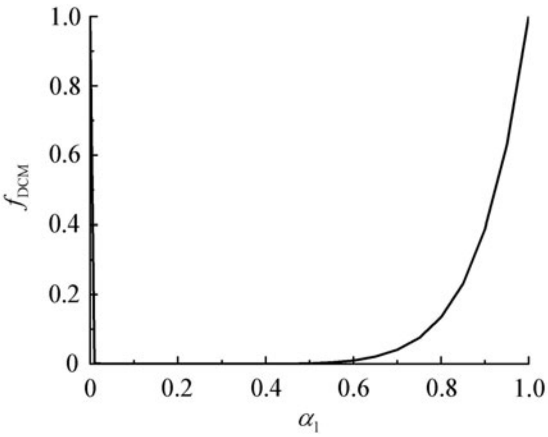

Fig. 1 Distribution of density correction function

It is reported that RANS models often yield excess eddy viscosity [17,23–25,34], which can suppress the large-scale unsteady motion. With the help of the filter function in Eq. (17) and density correction function in Eq. (19), it provides a systematic approach to reduce the excess eddy viscosity based on the local resolution or mixture density.

Besides the mathematics differences in filter function and density correction function, there also exists another major difference. The filter function mainly modifies the eddy viscosity away from the near-wall region, and this approach apparently does not correct the eddy viscosity directly near the wall region, where cavitation can occur easily, due to the use of wall function. As for the density correction function, generally speaking, it has no influence in the region away from the near-wall region since there is no phase change. However, the density correction function will start to work aggressively closer to the cavitation region around the near-wall region. We have noticed this difference between these two eddy viscosity correction functions regarding the affected region, and will provide a hybrid turbulence model according to the concept above

$$\mu_{\mathrm{T\_hybrid}} = \frac{C_\mu \rho_{\mathrm{m}} k^2}{\varepsilon} f_{\mathrm{hybrid}},$$

$$C_\mu = 0.09,$$

$$f_{\mathrm{hybrid}} = \chi(\rho_{\mathrm{m}}/\rho_{\mathrm{l}}) f_{\mathrm{FBM}} + [1 - \chi(\rho_{\mathrm{m}}/\rho_{\mathrm{l}})] f_{\mathrm{DCM}}, \tag{20}$$

$$\chi(\rho_{\mathrm{m}}/\rho_{\mathrm{l}}) = 0.5 + \tanh\left[\frac{C_1(0.6\rho_{\mathrm{m}}/\rho_{\mathrm{l}} - C_2)}{0.2(1 - 2C_2) + C_2}\right] \Big/ [2\tanh(C_1)], \tag{21}$$

where C_1 and C_2 was chosen to be 4 and 0.2, respectively.

The hybrid function χ (shown in Fig. 2) will blend filter-based approach and density correction method based on the local mixture density.

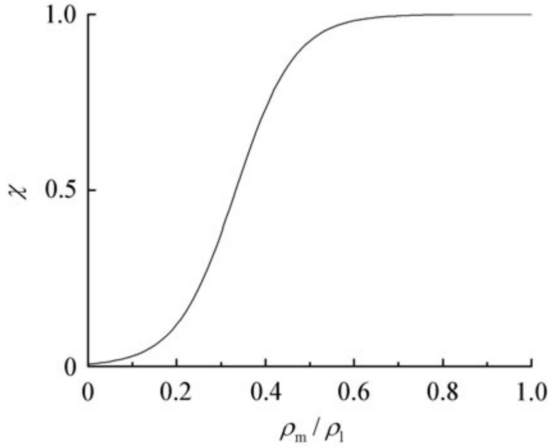

Fig. 2 Distribution of hybrid function χ

In current study, we will utilize the baseline k-ε turbulence model, modified k-ε turbulence model with filter function, density correct function and hybrid function (shown in Table 2) to investigate the impacts of turbulence models.

Table 2 Turbulence models used in the present study

Model	Turbulence eddy viscosity	Correct function f
Baseline model	$\mu_{\mathrm{T}} = \frac{C_\mu \rho_{\mathrm{m}} k^2}{\varepsilon} f$ $C_\mu = 0.09$	$f_{\mathrm{baseline}} = 1$
Filter-based model (FBM)		$f_{\mathrm{FBM}} = \min\left(1, \frac{\Delta \cdot \varepsilon}{k^{3/2}}\right)$
Density correction model (DCM)		$f_{\mathrm{DCM}} = \frac{\rho_{\mathrm{v}} + (\alpha_{\mathrm{l}})^n(\rho_{\mathrm{l}} - \rho_{\mathrm{v}})}{\rho_{\mathrm{v}} + \alpha_{\mathrm{l}}(\rho_{\mathrm{l}} - \rho_{\mathrm{v}})}$
Hybrid model		$f_{\mathrm{hybrid}} = \chi(\rho_{\mathrm{m}}/\rho_{\mathrm{l}}) f_{\mathrm{FBM}} + [1 - \chi(\rho_{\mathrm{m}}/\rho_{\mathrm{l}})] f_{\mathrm{DCM}}$ $\chi(\rho_{\mathrm{m}}/\rho_{\mathrm{l}}) = 0.5 + \frac{\tanh\left[\frac{C_1(0.6\rho_{\mathrm{m}}/\rho_{\mathrm{l}} - C_2)}{0.2(1 - 2C_2) + C_2}\right]}{2\tanh(C_1)}$

2.3 Numerical method

Detailed numerical procedures for the cavitation model and associated fluid dynamics equations adopted here utilize a modified pressure-based approach for large density jump as well as thermal effects, as reported in Refs. [17,21–25]. The controlled variation scheme (CVS) [21,32] is applied to discretize the convection scheme, and central difference is used for both pressure and diffusion terms. The CVS scheme can prevent the oscillations under sharp gradients caused by the phase change while preserving second-order accuracy elsewhere.

As for the boundary conditions, liquid volume fraction, velocity, temperature and turbulent quantities are specified at the inlet. For the outlet, pressure is fixed according to the corresponding cavitation number, and other flow variables are extrapolated. On the walls, pressure, liquid volume fraction, and turbulent quantities are extrapolated along with no-slip boundary condition [17,22].

Based on the eddy-to-laminar viscosity ratio at the inlet, $\mu_{\mathrm{T}}/\mu_{\mathrm{L}}\big|_{\mathrm{inlet}}$, the inlet turbulent quantities can be given as following

$$k = \frac{3}{2}(U_\infty I)^2, \qquad \varepsilon = \frac{k^2}{\nu_{\mathrm{L}}(\mu_{\mathrm{T}}/\mu_{\mathrm{L}}|_{\mathrm{inlet}})}, \tag{22}$$

where I is turbulence intensity, which is 0.02 here. Without experimental guidance, the inlet conditions are selected to allow the eddy-to-laminar viscosity ratio at the inlet, $\mu_{\mathrm{T}}/\mu_{\mathrm{L}}\big|_{\mathrm{inlet}}$, to vary [24,25].

In addition to the current approach employing body-fitted gridding, Cartesian grid-based multiphase fluid flow techniques are also being used [35–38]. These approaches offer advantage of treating moving interfaces with stationary grid. Their applicability is typically superior for flows with modest Reynolds numbers.

3 Results and discussion

The computational domain with 22 000 cells and boundary conditions are given according to the experimental setup in Refs. [1,17,39,40], which is shown in Fig. 3. The Clark-Y hydrofoil is placed in the center of water tunnel with angles of attack equal to 8°. The Reynolds number and the cavitation number are 7×10^5 and 0.8, respectively, and the flow is basically turbulent with cavity shedding under the current flow conditions. The filter size of FBM in Eq. (17) is chosen to be 1.5 times larger than the largest grid size in the computation domain, which is around $0.17C$. There are five model combinations listed in Table 3 to investigate the interactions between cavitation and turbulence models. Furthermore, the time-averaged drag coefficient, lift coefficient, and the primary main frequency obtained by numerical simulations from fast Fourier transfer (FFT) are also provided to compare with experimental data in Table 3.

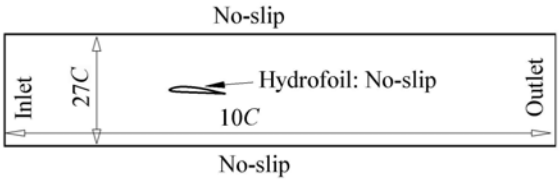

Fig. 3 Boundary conditions for Clark-Y hydrofoil

Table 3 Model combinations and corresponding behaviors Cavitation model: phenomenological model (Eq. (5)) and IDM (Eq. (8)) Turbulence model: baseline model (Eq. (16)), FBM (Eq. (17)), DCM (Eq. (19)), and hybrid model (Eq. (20))

Model combinations	Cavitation model	Turbulence model	Primary frequency/Hz	C_{l}	C_{d}
Phenomenological-baseline	Phenomenological	Baseline	27.3	0.682	0.118
Phenomenological-FBM	Phenomenological	FBM	27.3	0.669	0.114
Phenomenological-DCM	Phenomenological	DCM	35.1	0.543	0.121
Phenomenological-hybrid	Phenomenological	Hybrid	27.3	0.659	0.110
IDM-hybrid	IDM	Hybrid	39.1	0.641	0.112
Experimental data [39,40]			24.1	0.760	0.119

3.1 Time-averaged cavity visualization and flow structures

Figure 4 shows the time-averaged flow structure and cavity shape. It is clear that the cavitation structures consist of two parts, which are attached and detached cavity respectively. The attached cavity is located in the leading edge of the hydrofoil, while the detached cavity is formed due to the re-entrant jet and overlaps with the recirculation zone near the trailing edge. Figure 5 highlights the formation and significance of the re-entrant jet by the phenomenological-hybrid model to show the representative unsteady behaviors. The pressure inside the cavity is basically very low, which is close to the vapor pressure. When the adverse pressure gradient is strong enough to overcome the weaker momentum of the flow confined by the near-wall region, the re-entrant jet will form and push the flow toward the leading edge during the growth process of the attached cavity.

In Fig. 5a, a recirculation zone will consist of the re-entrant jet in the lower part and incoming flow from upstream in the upper part, and the front of the re-entrant jet will determine the cavity end. The recirculation zone will grow in size while the re-entrant jet pushing the attached cavity toward upstream will also become stronger, and then the cavity is detached in Fig. 5b with a low density region near the center of the recirculation zone. Finally, the detached cavity will be dissipated when it travels toward downstream. In this last stage, the re-entrant jet and the recirculation zone will become weaker, and meanwhile the attached cavity will grow up again to form the next cycle. The formation of re-entrant jet and its relationship to the cavity visualizations imply that the re-entrant jet plays a key role to trigger the unsteadiness of cavitation. The model combinations in Table 3 can basically capture these dynamic behaviors, and the difference between each combination will be discussed hereafter.

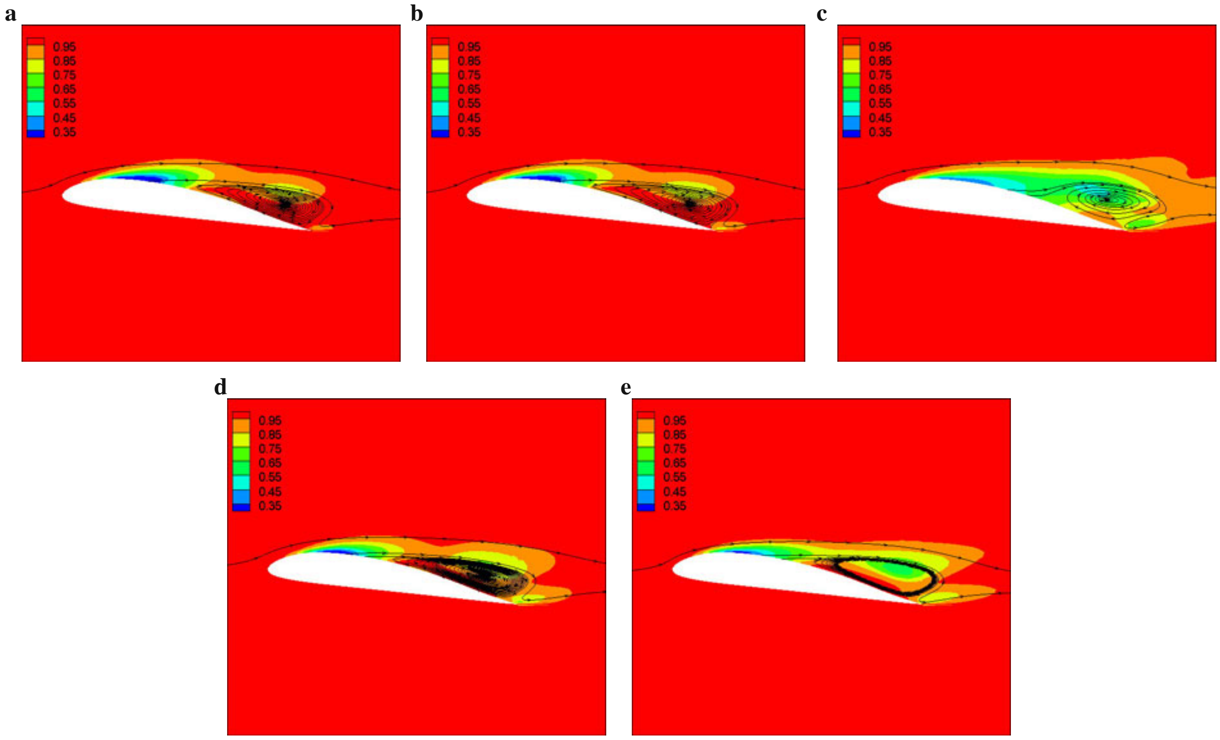

Fig. 4 Time-averaged liquid volume fraction contour and representative streamlines. **a** Phenomenological-baseline; **b** Phenomenological-FBM; **c** Phenomenological-DCM; **d** Phenomenological-hybrid; **e** IDM-hybrid

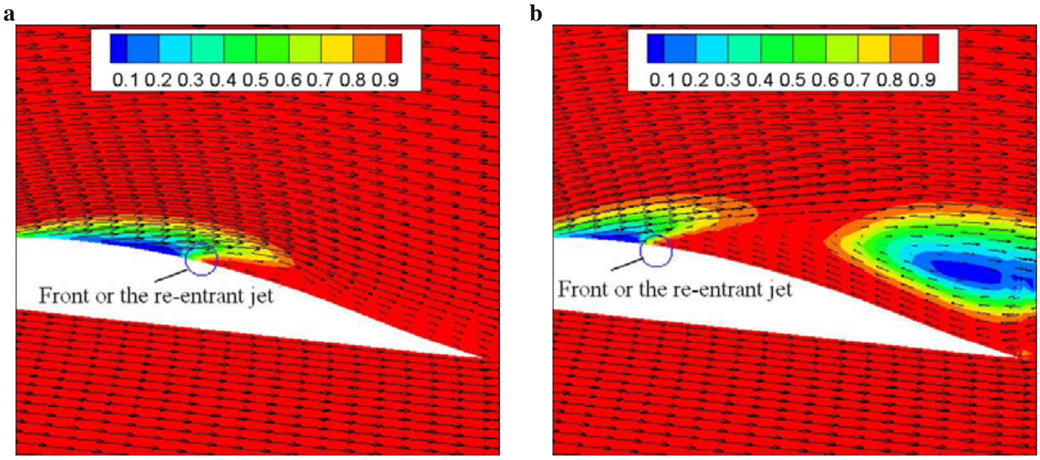

Fig. 5 The generation of re-entrant jet and detached cavity (by the phenomenological-hybrid model with black arrows as velocity vectors). **a** Formation of the re-entrant jet; **b** Highlight of the detached cavity

Overall speaking, from Fig. 4, the time-averaged attached cavity has a lower liquid volume fraction than that of the detached cavity. However, it does not necessarily mean the attached cavity always has a weaker cavitation phenomenon, but it does mean the attached cavity tends to stay longer right onto the leading edge within each cycle till the arrival of the re-entrant's front. The local velocity near the closure region and the center of the recirculation zone ($> 0.4U_\infty$) in Fig. 4 is always faster than that of the re-entrant jet ($-0.2U_\infty$ m/s at maximum) in our current flow condition. Therefore, the local velocity will sweep the detached cavity downstream faster than the velocity of re-entrant jet toward the leading edge, which leads to a longer existence of the attached cavity than the detached one.

3.1.1 Impact of turbulence models

(1) For the phenomenological-FBM model in Fig. 4b and the phenomenological-baseline model in Fig. 4a, the visualization of time-averaged cavity are very similar, and the only difference is that the size of the detached cavity is slightly larger for FBM. FBM and baseline turbulence model can perform comparably if the inlet turbulence quantities are already chosen properly [24]. Therefore, the time-averaged behaviors are very similar.

(2) For the phenomenological-DCM model in Fig. 4c, a bigger time-averaged cavity size is obtained. This is due to the fastest frequency (35.1 Hz) among all the cases in Table 3 by the phenomenological cavitation model (27.3 Hz for other combinations).

(3) For the phenomenological-hybrid model in Fig. 4d, there is apparently more weight placed from FBM than that from DCM because of the similarity between Figs. 4b and 4d. Besides, from Table 3, the frequencies are almost the same for the phenomenological-FBM and the phenomenological-hybrid model. The following two aspects can explain the similarity between the phenomenological-FBM and the phenomenological-hybrid model: first, the re-entrant jet, which triggers the shedding and unsteady motion, basically consists of high liquid volume fraction, and FBM is more influential than DCM model in this area; second, the hybrid model illustrated in Fig. 2 tends to use more portions from FBM (90% from FBM when liquid volume fraction is larger than 0.5). However, the detached cavity surely becomes more substantial in the phenomenological-hybrid model due to the contribution of DCM. The details will be discussed in Sects. 3.4 and 3.5.

3.2 Time-averaged velocity profiles

The mean x-direction velocity of the flow field is illustrated in Fig. 6. These time-averaged velocity profiles are tracked along the vertical direction at different locations, namely

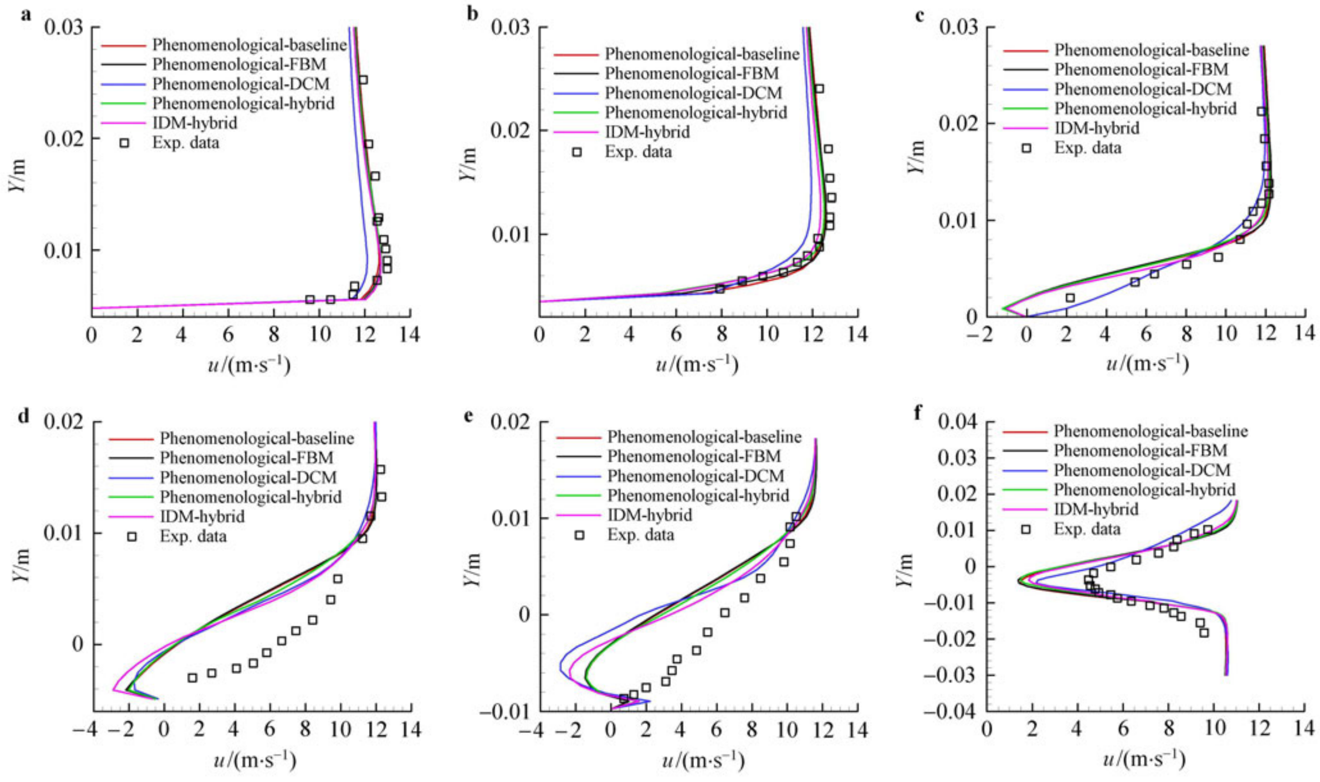

Fig. 6 Time-averaged x-direction velocity at different locations. **a** $x/C = 0.2$; **b** $x/C = 0.4$; **c** $x/C = 0.6$; **d** $x/C = 0.8$; **e** $x/C = 1.0$; **f** $x/C = 1.2$

x/C = 20%, 40%, 60%, 80%, 100%, and 120%. The difference between CFD results and experimental data becomes more substantial after the closure region. Overall speaking, the agreement is reasonable if we consider the difficulties in experimental measurement [40]. Even the time-averaged velocity profiles looks very similar, noticeable differences in instantaneous solutions do exist, especially in the near-wall region. Consequently, different lift forces result in Table 3. The instantaneous solution characteristics will be highlighted in Sect. 3.5.

3.3 Lift and drag coefficients

The history profile of lift coefficients is also shown in Fig. 7 to compare with the experimental data. The CFD results and experimental data are very comparable in Fig. 7 except the phenomenological-DCM and IDM-hybrid model, which apparently have faster frequencies in Table 3. Besides, the phenomenological-DCM model in Fig. 7b has the smallest overall lift coefficient, which results in the smallest mean lift coefficient in Table 3. Overall speaking, in Table 3, besides the phenomenological-DCM model, the agreements between CFD and experimental data in terms of mean lift and drag coefficient are good, especially the mean drag coefficient. From the time-averaged flow structures of the phenomenological-DCM in Fig. 4b and IDM-hybrid in Fig. 4e, the cavity changes the effective shape of the hydrofoil more substantially, which causes flow to separate more easily with faster frequencies in Table 3. Therefore, smaller mean lift force for these two model combinations is expected.

The frequencies of lift coefficients and their corresponding powers defined as the mean square value of the amplitude are both obtained by FFT analysis, as shown in Table 4. FFT for time histories of upper and lower wall pre-

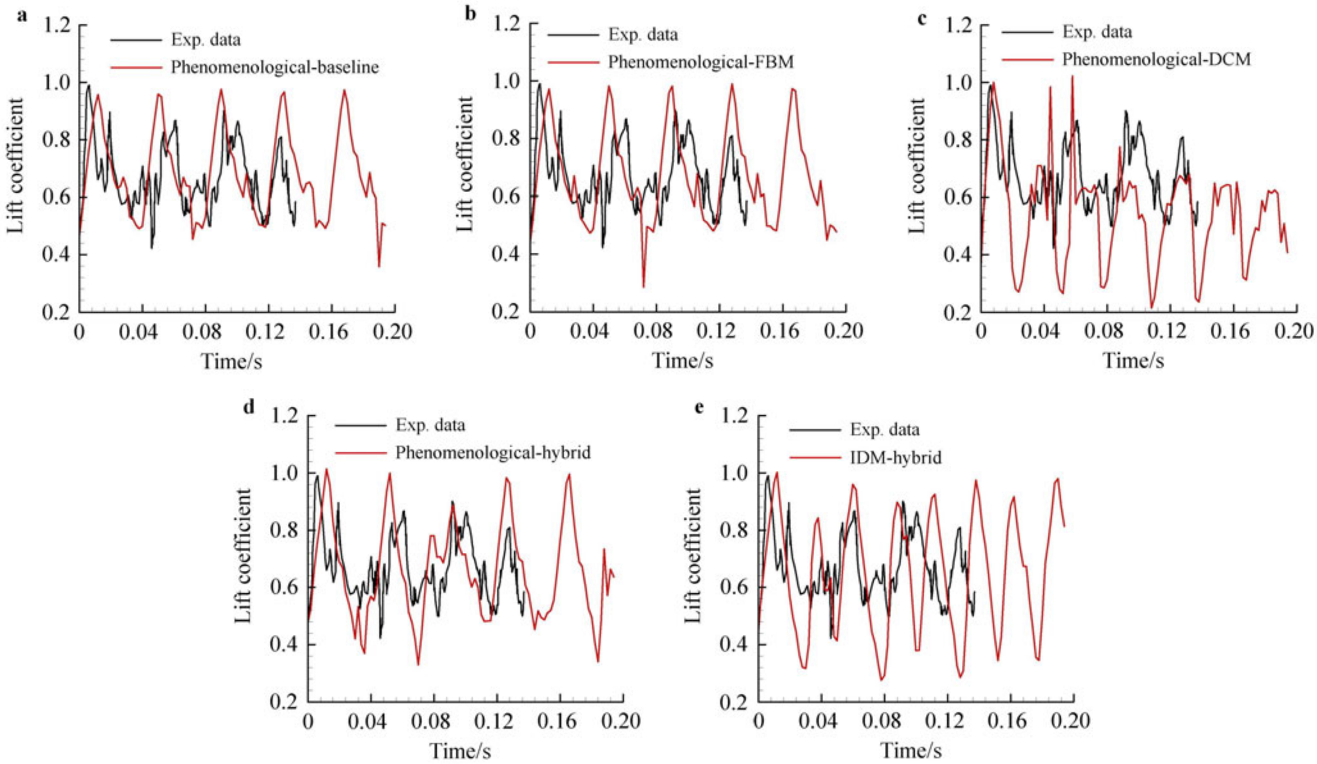

Fig. 7 History profile of lift coefficient. **a** Phenomenological-baseline; **b** Phenomenological-FBM; **c** Phenomenological-DCM; **d** Phenomenological-hybrid; **e** IDM-hybrid

Table 4 Frequency and power of lift coefficient

Model combination	Frequency 1	Power 1	Frequency 2	Power 2
Phenomenological-baseline	27.3	0.496	50.8	0.121
Phenomenological-FBM	27.3	0.578	50.8	0.134
Phenomenological-DCM	35.1	0.421	70.3	0.078
Phenomenological-hybrid	27.3	0.653	43.0	0.064
IDM-hybrid	23.4	0.119	39.1	1.235

ssure are also examined to investigate the source of these two main frequencies. The results show that the primary main frequencies with stronger power comes from the upper wall, and while another weaker main frequencies in Table 4 originate from the lower wall. Therefore, the cavitaion region on the upper wall determines the primary main frequencies listed in Table 3.

3.4 Time-averaged eddy viscosity

In Fig. 8a for the time-averaged eddy viscosity contour by the phenomenological-baseline model, there are two local maximum regions located near the leading edge of the hydrofoil and closure region of cavity separately. Filter function in Fig. 8b will filter out the larger portion of excess eddy viscosity in the regions near the leading edge and away from the cavity. FBM surely reduces the eddy viscosity near the closure region, but not as aggressive as those in the outer region. Basically, the filter function is not really invoked in this cavity region because of the resolution and the treatment of the near-wall region. However, FBM places a stronger reliance on DNS, the reduction of eddy viscosity is still expected even in the cavity region, and hence FBM in Fig. 8b only performs a minor reduction of eddy viscosity in the detached cavity region indirectly. Consequently, the time-averaged visualization of FBM in Fig. 4b has a slightly bigger detached cavity with a lower density inside due to the weaker dissipation of the eddy viscosity in this area.

For the phenomenological-DCM model in Fig. 8c, based on the liquid volume fraction, the eddy viscosity is reduced inside the cavity region while outer region keeps consistent value of that by baseline turbulence model in Fig. 8a. DCM directly performs an aggressive reduction of eddy viscosity, i.e. $f_{\mathrm{DCM}} = 0.4$ as $\alpha_1 = 0.9$ in Eq. (19), and it contrasts to FBM with only minor reduction of eddy viscosity in the detached cavity region. Therefore, the substantially lower eddy viscosity will tend to maintain the evaporation inside the detached cavity and have further shedding toward downstream. The smaller eddy viscosity, which covers entire cavity region in Fig. 8c, will give a stronger cavitation phenomenon in Fig. 4c and faster frequency in Table 3.

In Fig. 8d of the phenomenological-hybrid model, it is clear that more weight comes from FBM than that of DCM, which is also consistent to the analysis of Sect. 3.1. In the front part of the attached cavity, the density is still high, and thus FBM is mainly applied in this region by the hybrid function in Eq. (20) and Fig. 2. In the rear part of the attached cavity, DCM will start to dominate due to the low density in this region. However, the eddy viscosity of DCM and FBM in this region are very comparable. As for the closure region, the local maximum value in Fig. 8d is smaller than that of FBM in Fig. 8b. This contribution definitely comes from DCM. The detail of this aspect will be discussed in the next section.

As for the IDM-hybrid model in Fig. 8e, the eddy viscosity near the closure region is even lower than that of the phenomenological-hybrid model in Fig. 8d, which results in a bigger mean size of the detached cavity and a lower density inside in Fig. 4e.

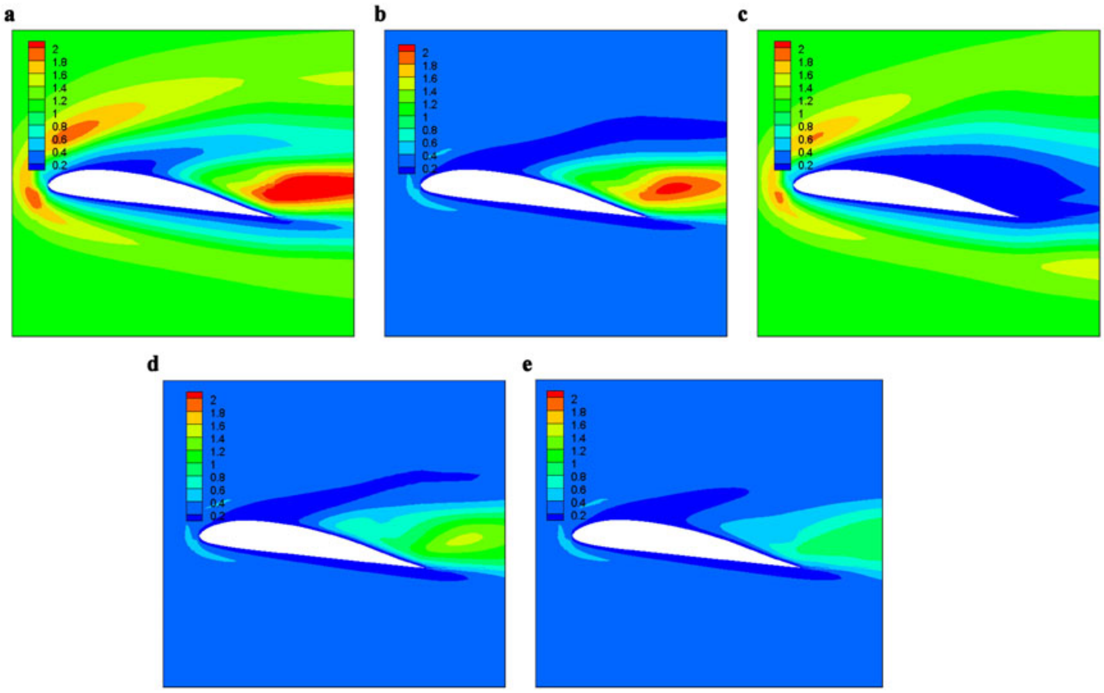

Fig. 8 Time-averaged eddy viscosity contours. **a** Phenomenological-baseline; **b** Phenomenological-FBM; **c** Phenomenological-DCM; **d** Phenomenological-hybrid; **e** IDM-hybrid

3.5 Instantaneous liquid volume fraction

The instantaneous contours of liquid volume fraction are compared with experimental data side by side in Fig. 9, and the interaction between cavitation and turbulence will be discussed based on the phenomenological cavitation model to highlight the impact of turbulence model. Although the frequencies are different between the CFD results and experimental data, the cavity visualizations are placed side by side according to 20%, 50%, 70%, and 90% of each corresponding cycle.

For the phenomenological-baseline and phenomenological-FBM model, the instantaneous contours of liquid volume fraction are very similar. We only show the results of the phenomenological-FBM model in Fig. 9a, the density inside the detached cavity still contains 60% of liquid phase during 50% to 70% cycle. The higher eddy viscosity of FBM near the closure region, as shown in Fig. 8b, will dissipate the detached cavity faster than that of DCM even before the density inside starts to largely consist of vapor phase. As the results, the phenomenological-baseline and phenomenological-FBM model can not capture the detached cavity during 90% of the cycle, and thus there will be a short period without cavitation in the entire flow fields. As for the attached cavity, the maximum cavity length is no more than 50%C.

For the phenomenological-DCM model in Fig. 9b, we can have better comparisons between CFD and experiment regarding the instantaneous cavity visualization. The detached cavity is well-captured around 90% of the cycle, which FBM fails to fulfill. During 20% of the cycle, the detached cavity from last cycle still prevails toward downstream in the right end of the first picture while the attached cavity remains under the growth process. During 50% of the cycle, before it is fully detached, the density inside this region already becomes very low, i.e. $\alpha_1 < 0.1$, which is much less than that of FBM. The stronger evaporation near the closure region, which is due to the small eddy viscosity in Fig. 8c, provides a more substantial detached cavity. Thus, the phenomenological-DCM model can capture the detached cavity in the last stage of the cycle, which is observed in the experiment. The detached cavity can prevail further even to 200%C, and this phenomenon is overestimated by comparing with the experimental data. As for the cavity length of the attached part, it can reach more than 80%C, and because of the longer existence of the detached cavity, the phase change always takes place somewhere in the flow domain.

As for the phenomenological-hybrid model in Fig. 9c, the features of every stage in experiment can be well-captured, including the detached cavity in the trailing edge of the last stage, and it will disappear before 120%C, which is more consistent to the observation experimentally. For the attached cavity, the maximum cavity can reach slightly more than 50%C, which is similar with that of FBM but much less

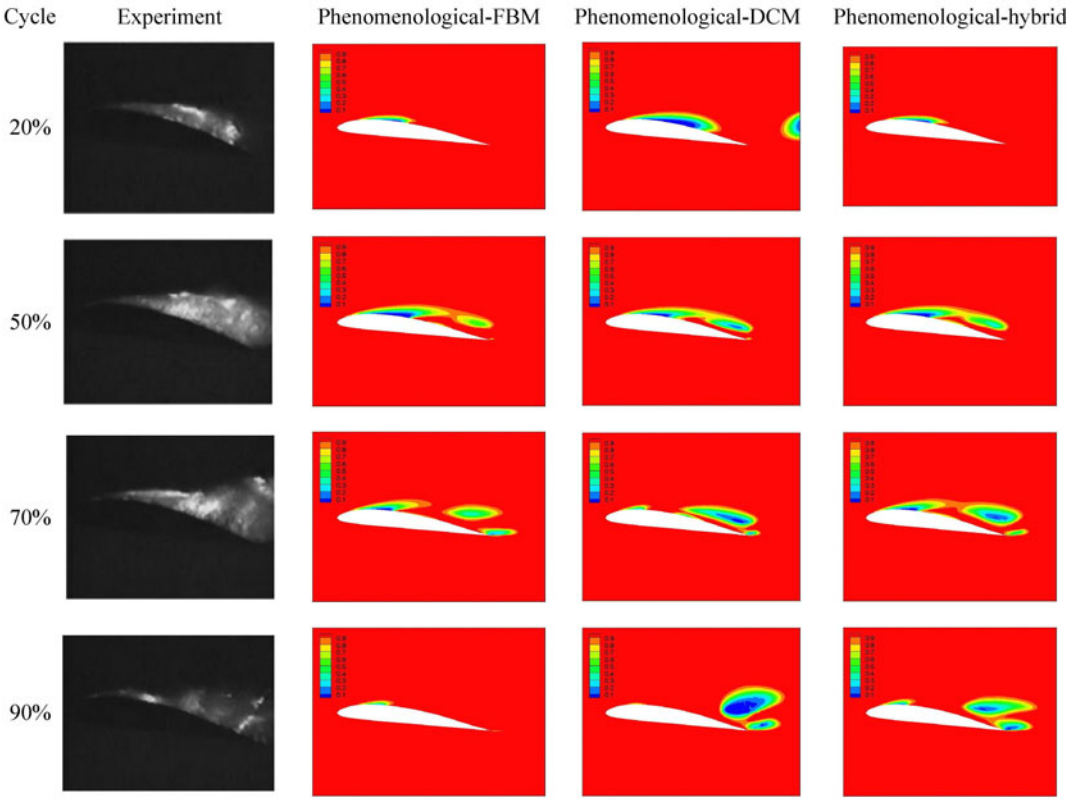

Fig. 9 Instantaneous contours of liquid volume fraction

than that of DCM model. The density is still high during 50% of the cycle before it is fully detached in Fig. 9c. However, this value is already enough to activate the contribution of DCM (44% from DCM as $\alpha_l = 0.35$). Therefore, a sudden reduction of eddy viscosity in the center of the detached cavity is obtained in Fig. 10a for the instantaneous eddy viscosity contour. In the surroundings except the center of the detached cavity, the contribution mainly comes from FBM. However, the sudden reduction due to the aggressive performance of DCM already can enhance the generation of the lower density-region during 70% of the cycle in Fig. 9c, i.e. $\alpha_l = 0.1$. The area with sudden reduction of eddy viscosity will grow in size, which is shown in Fig. 10b during the 70% of the cycle. This contribution from DCM enhances the detached cavity size compared with that of FBM, and weakens the dissipation so that the detached cavity is well-captured in the last stage.

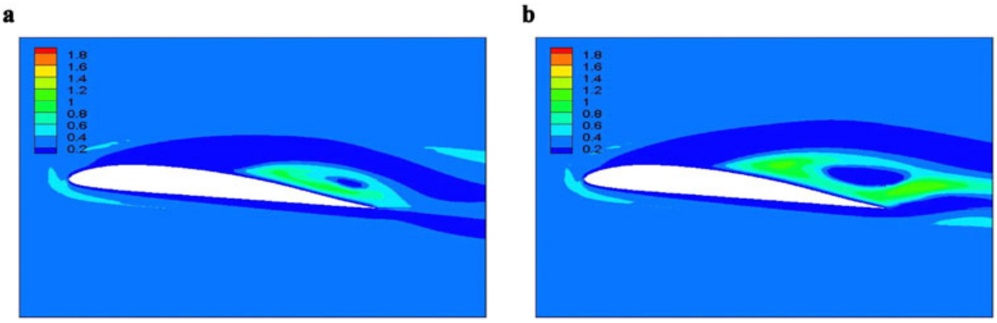

Fig. 10 Instantaneous contours of eddy viscosity by the phenomenological-hybrid model. **a** 50% of the cycle; **b** 70% of the cycle

3.6 Interpretation of C_{dest} and C_{prod} of alternative cavitation models

The impact and interactions between cavitation and turbulence models have been investigated in Sects. 3.4 and 3.5 based on the phenomenological model. In this section, the equivalent model parameters C'_{dest} and C'_{prod} can be obtained by comparing the phenomenological model in Eq. (5) and IDM in Eq. (8) as

$$C'_{\mathrm{dest}} = C'_{\mathrm{prod}} = \frac{0.5\rho_l U_\infty^2}{(\rho_l - \rho_v)(U_{v,n} - U_{I,n})^2}. \tag{23}$$

The hybrid turbulence model is used in this section, and there are two purposes for the analysis of C'_{dest} and C'_{prod}: (1) investigate when and where the evaporation and condensation processes become significant and (2) assess the differences and impacts between the phenomenological model and IDM.

3.6.1 Instantaneous cavity visualization of IDM

There are several noticeable aspects by comparing the cavity visualization shown in Fig. 11a of IDM and Fig. 9c of the phenomenological model: (1) during 50% of the cycle, IDM already can generate a low-density region before it is fully detached, and while this region of the phenomenological model still largely consists of water. (2) the sizes of the detached cavity and its low-density region are more substantial in Fig. 11 by IDM.

3.6.2 Instantaneous equivalent model parameters

The equivalent model parameters C'_{dest} and C'_{prod} are already normalized by $C_{\mathrm{dest}} = 1$ and $C_{\mathrm{prod}} = 80$ of the phenomenological model, respectively, in Figs. 11b and 11c. Since these two normalized model parameters are also highly consistent with the distributions of the cavitation sink and source terms in Eq. (8), $C'_{\mathrm{dest}}/C_{\mathrm{dest}}$ and $C'_{\mathrm{prod}}/C_{\mathrm{prod}}$ can be representative to the evaporation and condensation process when and where the evaporation and condensation processes become important in Fig. 11:

(1) During 20% of the cycle, the evaporation process largely concentrates in the low-density region in the attached cavity, and while the condensation process is confined to the interface of cavitation.

(2) During 50% of the cycle, the evaporation region travels to the cavity region above the trailing edge, and the value of $C'_{\mathrm{dest}}/C_{\mathrm{dest}}$ becomes greater, especially in the center of the low density region. The condensation process is still concentrated in the interface. The value of $C'_{\mathrm{prod}}/C_{\mathrm{prod}}$ in the region connecting the cavities between the leading edge and trailing edge also increases in this instant.

(3) During 70% of the cycle, the cavity above the trailing edge is fully detached, and the low density region inside this area grows in size, which is consistent to the distribution of $C'_{\mathrm{dest}}/C_{\mathrm{dest}}$ in Fig. 11b during this instant, and the value is even larger than that during 50% of the cycle. Since the fully-detachment is already fulfilled, the condensation area fully transports to the surroundings of the detached cavity in this instant.

(4) Finally during 90% of the cycle, the evaporation process in the center of the detached cavity becomes weaker, and the condensation area will become larger hereafter so that the detached cavity will collapse.

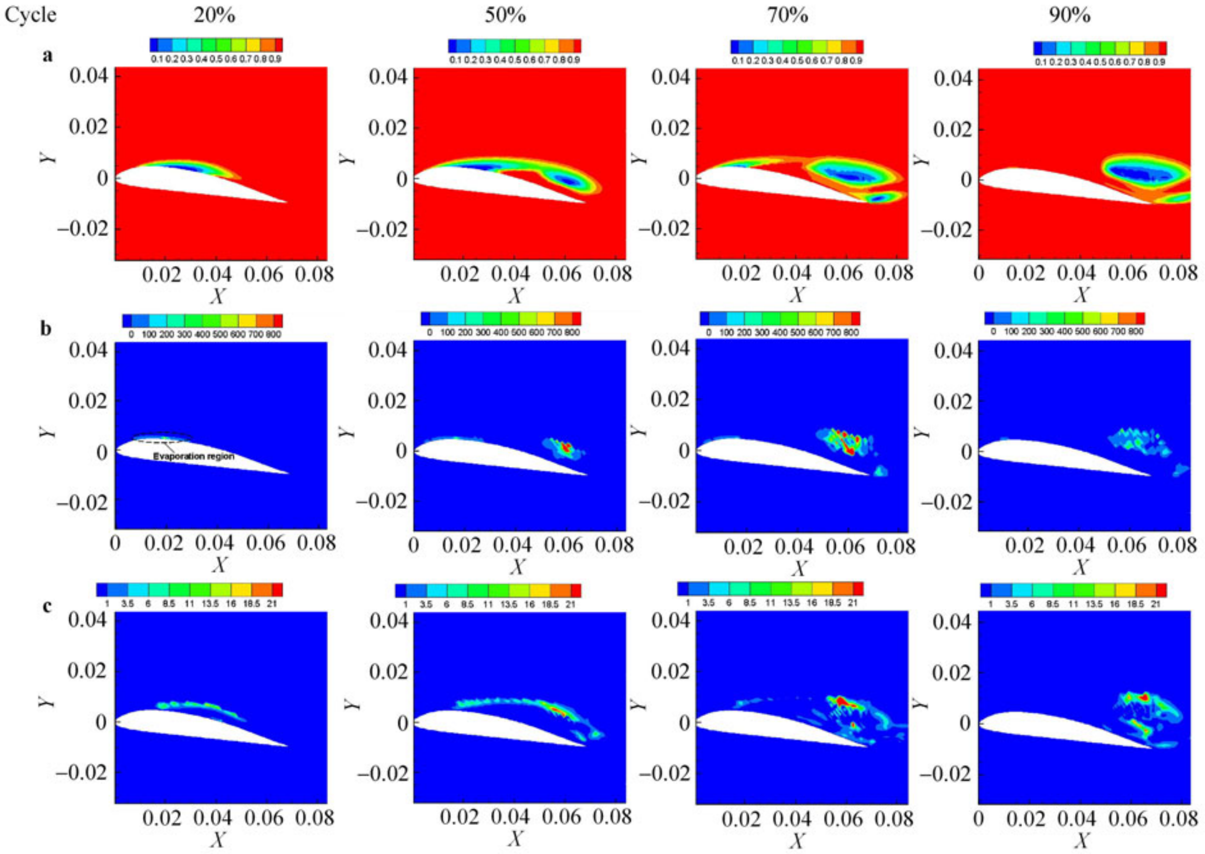

Fig. 11 **a** Instantaneous cavity visualizations and equivalent model parameters; **b** $C'_{\mathrm{dest}}/C_{\mathrm{dest}}$ of IDM; **c** $C'_{\mathrm{prod}}/C_{\mathrm{prod}}$ of IDM

The increase and decrease of $C'_{\mathrm{dest}}/C_{\mathrm{dest}}$ and $C'_{\mathrm{prod}}/C_{\mathrm{prod}}$ highlight the growth and decay of the cavitation phenomenon. Besides, the phase change process is more significant around the detached cavity than that of attached part under the current flow conditions.

3.6.3 Comparison of equivalent model parameters between the phenomenological model and IDM

Furthermore, the difference between the phenomenological model and IDM can be assessed. During 20% of the cycle, $C'_{\mathrm{dest}}/C_{\mathrm{dest}}$ varies from O(1) to O(2), and while $C'_{\mathrm{prod}}/C_{\mathrm{prod}}$ varies largely around O(1). As from 50% to 70% of the cycle, $C'_{\mathrm{dest}}/C_{\mathrm{dest}}$ increases from O(2) to O(3) with $C'_{\mathrm{prod}}/C_{\mathrm{prod}}$ around O(1). Finally during 90% of the cycle, $C'_{\mathrm{dest}}/C_{\mathrm{dest}}$ decays to O(2), and $C'_{\mathrm{prod}}/C_{\mathrm{prod}}$ still keeps around O(1). Therefore, a relatively stronger evaporation process is acquired, which results in a more substantial cavitation phenomenon, especially in the detached cavity, and hence the smaller lift force and faster frequency by IDM in Table 3 are expected due to more significant changes in the effective shape of the hydrofoil in Fig. 4e. IDM assumes the phase change takes place between the vapor and mixture phases, and thus it can lead to more significant cavitation phenomenon by the large density ratio between these two phases.

On the other hand, For IDM model, the equivalent reference time scale t'_{∞} can be also obtained by comparing the phenomenological model in Eq. (5) and IDM in Eq. (8). The parameter t_{∞}/t'_{∞} for evaporation and condensation process is the reciprocal of $C'_{\mathrm{dest}}/C_{\mathrm{dest}}$ and $C'_{\mathrm{prod}}/C_{\mathrm{prod}}$ for the corresponding phase change process, respectively. Therefore, t_{∞}/t'_{∞} is around O(1) to O(3) for the evaporation process and O(1) for the condensation process. It implies that the time scale t'_{∞} of IDM based on interfacial dynamics will be smaller than the mean flow time scale t_{∞}, especially for the evaporation process. Besides, it also reveals that a more precise definition for the time scale in IDM is needed.

Overall speaking, IDM can also capture the detached cavity visualization in Fig. 9 correctly. However, the performance of frequency and lift force in Table 3 is less accurate compared with those by the phenomenological model.

4 Summary and conclusions

In this study, the interaction of cavitation and turbulence model is investigated by different model combinations. The phenomenological model and IDM are used, as cavitation models, and as for the turbulence closure, FBM and DCM have been utilized to reduce the eddy viscosity systematically based on the meshing resolution and density, respectively. Moreover, hybrid model has blended FBM and DCM according to the density. The numerical results show that the difference between each model combination can be significantly different in time dependent processes even the time-averaged velocity profiles are reasonably similar.

The comparisons between each model combination are highlighted as follows:

(1) For the phenomenological-baseline and phenomenological-FBM model, comparable instantaneous and mean lift force as well as the primary main frequency is well-predicted. However, the detached cavity can not be well-captured. The only difference between these two is that a slightly larger detached cavity with lower density is obtained by FBM.
(2) For the phenomenological-DCM model, the mean lift force is the worst among these model combinations, and the predicted primary main frequency is faster than experimental observation. Moreover, the detached cavity is overestimated by DCM model.
(3) As for the phenomenological-hybrid model, the mean lift force is slightly worse than that of phenomenological-baseline and phenomenological-FBM model. However, the prediction of the primary main frequency is consistent with the experimental measurements, and the detached cavity is well-captured in this model combination.
(4) In the IDM-hybrid model, the mean lift force is lower, and the predicted primary main frequency is faster than the experimental measurements about 70%.

Therefore, no single model combination performs best in all aspects in terms of the force, primary main frequency, and detached cavity visualization.

In current study, hybrid model has placed more weight from FBM. However, the contribution of DCM becomes more substantial near the closure region, and it can significantly affect the dynamic behavior of the detached cavity.

The equivalent model parameter ratios between IDM and the phenomenological model are also investigated to highlight the transport of the phase change process and assess the differences between these two cavitation models. The evaporation and condensation region will travel based on the different stages within each cycle, and the phase change process is more significant around the detached cavity than that of attached part under the current flow conditions. Moreover, a relative stronger evaporation process is acquired by IDM, which results in a more substantial cavitation phenomenon, especially in the detached cavity, and hence the smaller lift force and faster frequency by IDM are expected. Besides, it also reveals that more precise definition for the time scale in IDM is needed for further investigation.

In summary, this study has applied a concept to blend different turbulence models and utilizes this idea to investigate the interaction between cavitation and turbulence. The phase change process is also examined by IDM model. Our current study provides the information for further modeling development.

References

1 Utturkar, Y., Wu, J., Wang, G., et al.: Recent progress in modeling of cryogenic cavitation for liquid rocket propulsion. Progress in Aerospace Sciences **41**(7), 558–608 (2005)
2 Knapp, R.T., Daily, J.W., Hammitt, F.G.: Cavitation. McGraw-Hill. New York (1970)
3 Brennen, C.E.: Cavitation and Bubble Dynamics. Oxford Engineering & Sciences Series 44, Oxford University Press (1995)
4 Joseph, D.D.: Cavitation in a flowing liquid. Phys. Review E **51**(3), 1649–1650 (1995)
5 Joseph, D.D.: Cavitation and the state of stress in a flowing liquid. Journal of Fluid Mechanics **366**, 367–378 (1998)
6 Kubota, A., Kato, H., Yamaguchi, H., et al.: Unsteady structure measurement of cloud cavitation on a foil section using conditional sampling technique. J. Fluid Eng-T. ASME **111**, 204–210 (1989)
7 Leroux, J.B., Astolfi, J.A., Billare, J.Y.: An experimental study of unsteady partial cavitation. ASME **26**, 94–101 (2004)
8 Kawanami, Y., Kato, H., Tanimura, M., et al.: Mechanism and control of cloud cavitation. J. Fluid Eng-T. ASME **119**, 788–794 (1997)
9 LaCallenaere, M., Franc, J.P., Michel, J.M., et al.: The cavitation instability induced by the development of a re-entrant jet. J. Fluid Mech. **444**, 223–256 (2001)
10 Gopalan, S., Katz, J.: Flow structure and modeling issues in the closure region of attached cavitation. Phys. Fluids **12**(4), 895–911 (2000)
11 Li, C.Y., Ceccio, S.L: Interaction of single travelling bubbles with the boundary layer and attached cavitation. J. Fluid Mech. **322**, 329–353 (1996)
12 Chen, Y., Hesiter, S. D.: A numerical treatment for attached cavitaition. J. Fluids Eng. **116**, 613–618 (1994)
13 Deshpande, M., Feng, J., Merkle, C.L.: Numerical modeling of the thermodynamic effects of cavitation. J. Fluids Eng. **119**, 420–427 (1997)
14 Huang, D., Zhuang, Y., Cai, R.: A computational method for cavitational flows based on energy conservation. IMechE **207**, 1333–1338 (2007)
15 Edward, J.R., Franklin, R.K., Liou, M.S.: Low-diffusion flux-splitting methods for real fluid flows with phase transition. AIAA Journal **38**(9), 1624–1633 (2000)
16 Delannoy, Y., Kueny, J.L.: Cavity flow prediction based on the Euler equations. ASM Cavitation and Multiphase Flow Forum. ASME-FED 98, 153–158 (1990)
17 Wu, J.Y., Wang, G.Y., Shyy, W.: Time-dependent turbulent cavutating flow computations with interfacial transport and filter-based models. International Journal for Numerical Methods in Fluids **49**(7), 739–761 (2005)
18 Merkle, C.L., Feng, J., Buelow, P.E.O.: Computational modeling of sheet cavitation. Proc. 3rd International Symposium on Cavitation, Grenoble, France 1998

19 Kunz, R.F., Boger, D.A., Stinebring, D.R., et al.: A preconditioned Navier–Stokes method for two phase flows with application to cavitation prediction. Comput. Fluids **29**, 849–875 (2000)

20 Hosangadi, A., Ahuja, V.: A numerical study of cavitation in cryogenic fluids. Journal of Fluids Engineering **127**, 267-281 (2005)

21 Senocak, I., Shyy, W.: Interfacial dynamics-based modeling of turbulent cavitating flows. Part 1: model development and steady-state computations. Int. J. Numer. Meth. Fluids **44**, 975–995 (2004)

22 Senocak, I., Shyy, W.: Interfacial dynamics-based modeling of turbulent cavitating flows. Part 2: time-dependent computations. Int. J. Numer. Meth. Fluids **44**, 997–1016 (2004)

23 Utturkar, Y., Wu, J., Wang, G., et al.: Recent progress in modeling of cryogenic cavitation for liquid rocket propulsion. Progress in Aerospace Sciences **41**(7), 558–608 (2005)

24 Tseng, C., Shyy, W.: Modeling for isothermal and cryogenic cavitation. Int. J. Heat Mass Transfer **53**, 513–525 (2010)

25 Tseng, C., Shyy, W.: Surrogate-based modeling of cryogenic turbulent cavitating flows. CAV2009, Paper No. 77. Proceedings of the 7th International Symposium on Cavitation, August 17-22, 2009, Ann Arbor, Michigan, USA

26 Li, X., Wang, G., Yu, Z., et al.: Multiphase fluid dynamics and transport processes of low capillary number cavitating flows. Acta Mechanica Sinica **25**, 161–172 (2008)

27 Singhal, A.k., Li, H., Athavale, M.M., et al.: Mathematical basis and validation of the full cavitation model. J. Fluids Eng. **124**(3), 617–625 (2002)

28 Hosangadi, A., Ahuja, V.A.: Numerical of cavitation in cryogenic fluids. Part 2 — new unsteady model for dense cloud. cavitation. 6th International Symposium on Cavitation, Wageningen, Netherlands. Sep. 2006

29 Hosangadi, A., Ahuja, V., Ungewitter, R.J.: Simulations of rotational cavitation instabilities in the SSME LPFP inducer. In: 43rd AIAA/ASME/SAE/ASEE Joint Propulsion Conference & Exhibit; 1-16. 2007

30 Coutier-Delgosha1, R., Fortes-Patella, O., Reboud, J.L.: Evaluation of the turbulence model influence on the numerical simulations of unsteady cavitation. Journal of Fluids Engineering **125**, 38–45 (2003)

31 Ahuja, V., Hosangadi, A., Arunajatesan, S.: Simulations of cavitating flows using hybrid unstructured meshes. Journal of Fluids Engineering **123**, 123–331 (2001)

32 Shyy, W., Thakur, S.S., Ouyang, H., et al.: Computational Techniques for Complex Transport Phenomenon. Cambridge University Press (2007)

33 Launder, B.E., Spalding, D.B.: The numerical computation of turbulent flow. Comp. Meth. Appl. Mech. Eng. **3**, 269–289 (1974)

34 Johansen, S.T., Wu, J.Y., Shyy, W.: Filter based unsteady RANS computational. International Journal of Heat and Fluid Flow **25**, 10–21 (2005)

35 Shyy, W., Udaykumar, H.S., Rao, M.M., et al.: Computational Fluid Dynamics with Moving Boundaries, Taylor & Francis, Washington, DC (1996); Dover, New York (2007)

36 Francois, M., Shyy, W.: Computations of drop dynamics with the immersed boundary method; Part 1 — numerical algorithm and buoyancy induced effect. Numerical Heat Transfer, Part B **44**, 101–118 (2003)

37 Francois, M., Shyy, W.: Computations of drop dynamics with the immersed boundary method; Part 2 — drop impact and heat transfer. Numerical Heat Transfer, Part B **44**, 119–143 (2003)

38 Ye, T., Shyy, W., Chung, J.C.: A fixed-grid, sharp-interface method for bubble dynamics and phase change. Journal of Computational Physics **174**, 781–815 (2001)

39 Wang, G., Zhang, B., Huang, B., et al.: Unsteady dynamics of cloudy cavitating flows around a hydrofoil. CAV2009, Paper No. 9. In: Proceedings of the 7th International Symposium on Cavitation, August 17-22, 2009, Ann Arbor, Michigan, USA

40 Wang, G., Senocak, I., Shyy, W., et al.: Dynamics of attached turbulent cavitating flows. Progress in Aerospace Sciences **37**, 551–581 (2001)